Available online at www.sciencedirect.com
SCIENCE DIRECT®
International Journal of Heat and Mass Transfer 49 (2006) 1430–1441
International Journal of HEAT and MASS TRANSFER
www.elsevier.com/locate/ijhmt

Natural convection in a square cavity filled with a porous medium: Effects of various thermal boundary conditions

Tanmay Basak [a], S. Roy [b], T. Paul [b], I. Pop [c,*]

[a] Department of Chemical Engineering, Indian Institute of Technology Madras, Chennai 600 036, India
[b] Department of Mathematics, Indian Institute of Technology Madras, Chennai 600 036, India
[c] Faculty of Mathematics, University of Cluj, R-3400 Cluj, CP 253, Romania

Received 1 March 2005; received in revised form 14 September 2005
Available online 26 January 2006

Abstract

Natural convection flows in a square cavity filled with a porous matrix has been studied numerically using penalty finite element method for uniformly and non-uniformly heated bottom wall, and adiabatic top wall maintaining constant temperature of cold vertical walls. Darcy–Forchheimer model is used to simulate the momentum transfer in the porous medium. The numerical procedure is adopted in the present study yields consistent performance over a wide range of parameters (Rayleigh number Ra, $10^3 \leqslant Ra \leqslant 10^6$, Darcy number Da, $10^{-5} \leqslant Da \leqslant 10^{-3}$, and Prandtl number Pr, $0.71 \leqslant Pr \leqslant 10$) with respect to continuous and discontinuous thermal boundary conditions. Numerical results are presented in terms of stream functions, temperature profiles and Nusselt numbers. Non-uniform heating of the bottom wall produces greater heat transfer rate at the center of the bottom wall than uniform heating case for all Rayleigh numbers but average Nusselt number shows overall lower heat transfer rate for non-uniform heating case. It has been found that the heat transfer is primarily due to conduction for $Da \leqslant 10^{-5}$ irrespective of Ra and Pr. The conductive heat transfer regime as a function of Ra has also been reported for $Da \geqslant 10^{-4}$. Critical Rayleigh numbers for conduction dominant heat transfer cases have been obtained and for convection dominated regimes the power law correlations between average Nusselt number and Rayleigh numbers are presented.

Keywords: Natural convection; Square cavity; Porous medium; Penalty finite element method

1. Introduction

The convective motion driven by buoyancy forces is well-known natural phenomena, and has attracted many researchers' interests. In this context, buoyancy driven phenomena in porous media are actively under investigation. Non-Darcy effects on natural convection in porous media have received a great deal of attention in recent years. This is due to a large number of technical applications, such as, fluid flow in geothermal reservoirs, separation processes in chemical industries, dispersion of chemical contaminants through water saturated soil, solidification of casting, migration of moisture in grain storage system, crude oil production, etc. Comprehensive literature survey concerned with this subject is given by Kaviany [1], Nield and Bejan [2], Ingham and Pop [3], Vafai [4], Pop and Ingham [5], Bejan and Kraus [6], Ingham et al. [7] and Bejan et al. [8].

The buoyancy driven convection in a porous cavity heated differentially in the horizontal side has been analyzed by Walker and Homsy [9] by a number of different techniques. The results obtained are fairly good agreement with each other as well as experimental results. The Brinkman-extended Darcy model has been considered by Tong and Subramanian [10], and Lauriat and Prasad [11] to examine the buoyancy effects on free convection in a vertical cavity. This model has been introduced by Brinkman [12] in order to account for the transition from Darcy flow

* Corresponding author. Tel.: +40 264 594315; fax: +40 264 591906.
E-mail addresses: tanmay@iitm.ac.in (T. Basak), sjroy@iitm.ac.in (S. Roy), popi@math.ubbcluj.ro (I. Pop).

0017-9310/$ - see front matter © 2005 Elsevier Ltd. All rights reserved.
doi:10.1016/j.ijheatmasstransfer.2005.09.018

Nomenclature

Da	Darcy number
g	acceleration due to gravity (ms^{-2})
J	Jacobian of residual equations
k	thermal conductivity ($W\,m^{-1}\,K^{-1}$)
K	permeability of the porous medium
L	side of the square cavity (m)
N	total number of nodes
Nu	local Nusselt number
p	pressure (Pa)
P	dimensionless pressure
Pr	Prandtl number
R	residual of weak form
Ra	Rayleigh number
T	temperature (K)
T_h	temperature of hot bottom wall (K)
T_c	temperature of cold vertical wall (K)
u	*x* component of velocity
U	*x* component of dimensionless velocity
v	*y* component of velocity
V	*y* component of dimensionless velocity
X	dimensionless distance along *x* coordinate
Y	dimensionless distance along *y* coordinate

Greek symbols

α	thermal diffusivity ($m^2\,s^{-1}$)
β	volume expansion coefficient (K^{-1})
γ	penalty parameter
θ	dimensionless temperature
ν	kinematic viscosity ($m^2\,s^{-1}$)
ρ	density ($kg\,m^{-3}$)
Φ	basis functions
ψ	stream function
ξ	horizontal coordinate in a unit square
η	vertical coordinate in a unit square

Subscripts

b	bottom wall
i	residual number
k	node number
s	side wall

Superscript

n	Newton iterative index

to highly viscous flow (without porous matrix), in the limit of extremely high permeability. However, Brinkman model does not account adequately for the transition from porous medium flow to pure fluid flow as the permeability of the porous medium increases. A model that bridges the entire gap between the Darcy and Navier Stokes equations is the Darcy–Forchheimer model which was developed by Vafai and Tien [13]. It is known that the Darcy's law is an empirical formula relating the pressure gradient, the gravitational force and the bulk viscous resistance in porous media. Thus, the mathematical formulations based on Dracy's law will neglect the effects of a solid boundary or the inertia forces on fluid flow and heat transfer through porous media. In general, the inertia and boundary effects become significant when the fluid velocity is high and the heat transfer is considered in the near wall region [14]. In addition, the Darcy–Forchheimer model describes the effect of inertia as well as viscous forces in porous media and was used by Poulikakos and Bejan [15,16], Beckermann et al. [17], and Lauriat and Prasad [18] to examine the natural convection in a vertical porous layer and in a vertical enclosure filled with a porous medium. Further, natural convection in a square enclosure filled with a fluid saturated porous medium using a thermal non-equilibrium model has been investigated by Mohammad [19] for Brinkman-extended Darcy flow and by Baytas and Pop [20] for Darcy flow. Also, the effect of viscous dissipation has been considered for Darcy model by Saeid and Pop [21]. In contrast, very few investigations have been made in the past to focus on natural convection in porous medium due to uniform heating from below as reported by Horne and O'sullivan [22], Caltagirone [23] and Straus [24].

The aim of the present investigation is to study a natural convective flow in a square cavity filled with a fluid saturated porous medium when the bottom wall is heated (uniformly and non-uniformly) and the top wall is well insulated, while the two vertical walls are cooled by means of two constant temperature baths (see Fig. 1). The Darcy–Forchheimer model without the Forchheimer's inertia term

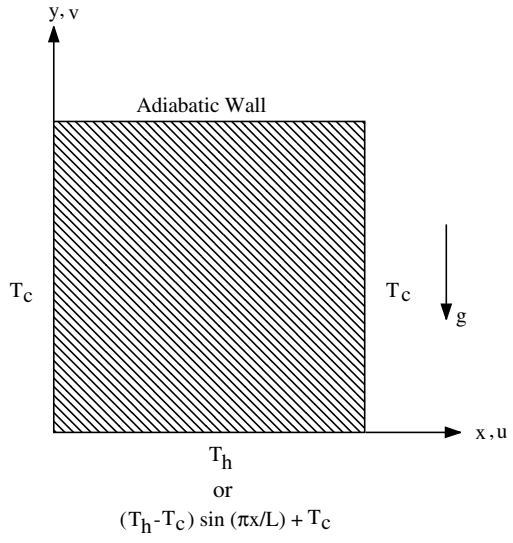

Fig. 1. Schematic diagram of the physical system.

has been adopted. In case of uniformly heated bottom wall, the finite discontinuities in temperature distribution appear at the edges of the bottom wall. The discontinuities can be removed by choosing a non-uniform temperature distribution along the bottom wall (i.e., non-uniformly heated bottom wall) as discussed by Minkowycz et al. [25], where the investigation is made for a mixed convection flow on a heated or cooled vertical plate. In our current study, we have used Galerkin finite element method with penalty parameter to solve the non-linear coupled partial differential equations governing flow and temperature fields for both uniform and non-uniform temperature distribution prescribed at the bottom wall. The momentum transfer in the porous medium is based on the Darcy–Forchheimer model. Numerical results are obtained to display the circulations and temperature distributions within the cavity and the heat transfer rate at the heated wall in terms of local and average Nusselt numbers.

2. Governing equations

Consider a fluid saturated porous medium enclosed in a square cavity of side L. It is assumed that the bottom wall is heated uniformly and non-uniformly while the top wall is well insulated and the vertical walls are cooled to a constant temperature. The geometry of this cavity together with the coordinate system is illustrated in Fig. 1. The physical properties are assumed to be constant except the density in the buoyancy force term which is satisfied by the Boussinesq's approximation. Further, it is assumed that the temperature of the fluid phase is equal to the temperature of the solid phase everywhere in the porous region, and local thermal equilibrium (LTE) model is applicable in the present investigation [2]. Also, a velocity square term could be incorporated in the momentum equations to model the inertia effect which is more important for non-Darcy effect on the convective boundary layer flow over the surface of a body embedded in a high porosity media. However, we have neglected this term in the present study because we are dealing with the natural convection flow in a cavity filled with a porous medium. Under these assumptions and following Vafai and Tien [13] with the Forchheimer's inertia term neglected, the governing equations for steady two-dimensional natural convection flow in the porous cavity using conservation of mass, momentum and energy can be written as: [26]

$$\frac{\partial u}{\partial x}+\frac{\partial v}{\partial y}=0, \tag{1}$$

$$u\frac{\partial u}{\partial x}+v\frac{\partial u}{\partial y}=-\frac{1}{\rho}\frac{\partial p}{\partial x}+\nu\left(\frac{\partial^2 u}{\partial x^2}+\frac{\partial^2 u}{\partial y^2}\right)-\frac{\nu}{K}u, \tag{2}$$

$$u\frac{\partial v}{\partial x}+v\frac{\partial v}{\partial y}=-\frac{1}{\rho}\frac{\partial p}{\partial y}+\nu\left(\frac{\partial^2 v}{\partial x^2}+\frac{\partial^2 v}{\partial y^2}\right)-\frac{\nu}{K}v+g\beta(T-T_c), \tag{3}$$

$$u\frac{\partial T}{\partial x}+v\frac{\partial T}{\partial y}=\alpha\left(\frac{\partial^2 T}{\partial x^2}+\frac{\partial^2 T}{\partial y^2}\right), \tag{4}$$

with boundary conditions

$$\begin{aligned}&u(x,0)=u(x,L)=u(0,y)=u(L,y)=0,\\&v(x,0)=v(x,L)=v(0,y)=v(L,y)=0,\\&T(x,0)=T_h,\quad \text{or}\quad T(x,0)=(T_h-T_c)\sin\left(\frac{\pi x}{L}\right)+T_c,\\&\frac{\partial T}{\partial y}(x,L)=0,\quad T(0,y)=T(L,y)=T_c,\end{aligned} \tag{5}$$

where x and y are the distances measured along the horizontal and vertical directions, respectively; u and v are the velocity components in the x- and y- directions, respectively; T denotes the temperature; ν and α are kinematic viscosity and thermal diffusivity, respectively; K is the medium permeability; p is the pressure and ρ is the density; T_h and T_c are the temperatures at hot bottom wall and cold vertical walls, respectively; L is the side of the square cavity.

Using the following change of variables,

$$\begin{aligned}&X=\frac{x}{L},\quad Y=\frac{y}{L},\quad U=\frac{uL}{\alpha},\quad V=\frac{vL}{\alpha},\quad \theta=\frac{T-T_c}{T_h-T_c}\\&P=\frac{pL^2}{\rho\alpha^2},\quad Pr=\frac{\nu}{\alpha},\quad Da=\frac{K}{L^2},\quad Ra=\frac{g\beta(T_h-T_c)L^3Pr}{\nu^2}\end{aligned} \tag{6}$$

the governing equations (1)–(4) reduce to non-dimensional form:

$$\frac{\partial U}{\partial X}+\frac{\partial V}{\partial Y}=0, \tag{7}$$

$$U\frac{\partial U}{\partial X}+V\frac{\partial U}{\partial Y}=-\frac{\partial P}{\partial X}+Pr\left(\frac{\partial^2 U}{\partial X^2}+\frac{\partial^2 U}{\partial Y^2}\right)-\frac{Pr}{Da}U, \tag{8}$$

$$U\frac{\partial V}{\partial X}+V\frac{\partial V}{\partial Y}=-\frac{\partial P}{\partial Y}+Pr\left(\frac{\partial^2 V}{\partial X^2}+\frac{\partial^2 V}{\partial Y^2}\right)-\frac{Pr}{Da}V+RaPr\theta, \tag{9}$$

$$U\frac{\partial \theta}{\partial X}+V\frac{\partial \theta}{\partial Y}=\frac{\partial^2 \theta}{\partial X^2}+\frac{\partial^2 \theta}{\partial Y^2} \tag{10}$$

with the boundary conditions

$$\begin{aligned}&U(X,0)=U(X,1)=U(0,Y)=U(1,Y)=0,\\&V(X,0)=V(X,1)=V(0,Y)=V(1,Y)=0,\\&\theta(X,0)=1,\quad \text{or}\quad \theta(X,0)=\sin(\pi X),\\&\theta(0,Y)=\theta(1,Y)=0,\quad \frac{\partial\theta}{\partial Y}(X,1)=0.\end{aligned} \tag{11}$$

Here, X and Y are dimensionless coordinates varying along horizontal and vertical directions, respectively; U and V are, dimensionless velocity components in the X- and Y-directions, respectively; θ is the dimensionless temperature; P is the dimensionless pressure; Ra, Pr and Da are Rayleigh, Prandtl and Darcy numbers, respectively.

3. Solution procedure

The momentum and energy balance Eqs. (8)–(10) are solved using the Galerkin finite element method. The

continuity Eq. (7) will be used as a constraint due to mass conservation and this constraint may be used to obtain the pressure distribution [27,28]. In order to solve Eqs. (8)–(10), we use the penalty finite element method where the pressure P is eliminated by a penalty parameter γ and the incompressibility criteria given by Eq. (7) [28] which results in

$$P = -\gamma\left(\frac{\partial U}{\partial X} + \frac{\partial V}{\partial Y}\right). \tag{12}$$

The continuity Eq. (7) is automatically satisfied for large values of γ. Typical values of γ that yield consistent solutions are 10^7 [27,28].

Using Eq. (12), the momentum balance Eqs. (8) and (9) reduce to

$$U\frac{\partial U}{\partial X} + V\frac{\partial U}{\partial Y} = \gamma\frac{\partial}{\partial X}\left(\frac{\partial U}{\partial X} + \frac{\partial V}{\partial Y}\right) + Pr\left(\frac{\partial^2 U}{\partial X^2} + \frac{\partial^2 U}{\partial Y^2}\right) - \frac{Pr}{Da}U, \tag{13}$$

and

$$U\frac{\partial V}{\partial X} + V\frac{\partial V}{\partial Y} = \gamma\frac{\partial}{\partial Y}\left(\frac{\partial U}{\partial X} + \frac{\partial V}{\partial Y}\right) + Pr\left(\frac{\partial^2 V}{\partial X^2} + \frac{\partial^2 V}{\partial Y^2}\right) - \frac{Pr}{Da}V + RaPr\theta. \tag{14}$$

Expanding the velocity components (U,V) and temperature (θ) using basis set $\{\Phi_k\}_{k=1}^N$ as,

$$U \approx \sum_{k=1}^{N} U_k\Phi_k(X,Y), \quad V \approx \sum_{k=1}^{N} V_k\Phi_k(X,Y) \quad \text{and} \quad \theta \approx \sum_{k=1}^{N} \theta_k\Phi_k(X,Y), \tag{15}$$

for

$$0 \leqslant X, Y \leqslant 1,$$

the Galerkin finite element method yields the following non-linear residual equations for Eqs. (13), (14) and (10), respectively, at nodes of internal domain Ω:

$$R_i^{(1)} = \sum_{k=1}^{N} U_k \int_\Omega \left[\left(\sum_{k=1}^{N} U_k\Phi_k\right)\frac{\partial\Phi_k}{\partial X} + \left(\sum_{k=1}^{N} V_k\Phi_k\right)\frac{\partial\Phi_k}{\partial Y}\right]\Phi_i\,\mathrm{d}X\mathrm{d}Y + \gamma\left[\sum_{k=1}^{N} U_k\int_\Omega \frac{\partial\Phi_i}{\partial X}\frac{\partial\Phi_k}{\partial X}\,\mathrm{d}X\mathrm{d}Y + \sum_{k=1}^{N} V_k\int_\Omega \frac{\partial\Phi_i}{\partial X}\frac{\partial\Phi_k}{\partial Y}\,\mathrm{d}X\mathrm{d}Y\right] + Pr\sum_{k=1}^{N} U_k\int_\Omega\left[\frac{\partial\Phi_i}{\partial X}\frac{\partial\Phi_k}{\partial X} + \frac{\partial\Phi_i}{\partial Y}\frac{\partial\Phi_k}{\partial Y}\right]\mathrm{d}X\mathrm{d}Y + \frac{Pr}{Da}\int_\Omega\left(\sum_{k=1}^{N} U_k\Phi_k\right)\Phi_i\,\mathrm{d}X\mathrm{d}Y \tag{16}$$

$$R_i^{(2)} = \sum_{k=1}^{N} V_k \int_\Omega \left[\left(\sum_{k=1}^{N} U_k\Phi_k\right)\frac{\partial\Phi_k}{\partial X} + \left(\sum_{k=1}^{N} V_k\Phi_k\right)\frac{\partial\Phi_k}{\partial Y}\right]\Phi_i\,\mathrm{d}X\mathrm{d}Y + \gamma\left[\sum_{k=1}^{N} U_k\int_\Omega \frac{\partial\Phi_i}{\partial Y}\frac{\partial\Phi_k}{\partial X}\,\mathrm{d}X\mathrm{d}Y + \sum_{k=1}^{N} V_k\int_\Omega \frac{\partial\Phi_i}{\partial Y}\frac{\partial\Phi_k}{\partial Y}\,\mathrm{d}X\mathrm{d}Y\right] + Pr\sum_{k=1}^{N} V_k\int_\Omega\left[\frac{\partial\Phi_i}{\partial X}\frac{\partial\Phi_k}{\partial X} + \frac{\partial\Phi_i}{\partial Y}\frac{\partial\Phi_k}{\partial Y}\right]\mathrm{d}X\mathrm{d}Y + \frac{Pr}{Da}\int_\Omega\left(\sum_{k=1}^{N} V_k\Phi_k\right)\Phi_i\,\mathrm{d}X\mathrm{d}Y - RaPr\int_\Omega\left(\sum_{k=1}^{N}\theta_k\Phi_k\right)\Phi_i\,\mathrm{d}X\mathrm{d}Y \tag{17}$$

and

$$R_i^{(3)} = \sum_{k=1}^{N}\theta_k\int_\Omega\left[\left(\sum_{k=1}^{N} U_k\Phi_k\right)\frac{\partial\Phi_k}{\partial X} + \left(\sum_{k=1}^{N} V_k\Phi_k\right)\frac{\partial\Phi_k}{\partial Y}\right]\Phi_i\,\mathrm{d}X\mathrm{d}Y + \sum_{k=1}^{N}\theta_k\int_\Omega\left[\frac{\partial\Phi_i}{\partial X}\frac{\partial\Phi_k}{\partial X} + \frac{\partial\Phi_i}{\partial Y}\frac{\partial\Phi_k}{\partial Y}\right]\mathrm{d}X\mathrm{d}Y. \tag{18}$$

Bi-quadratic basis functions with three point Gaussian quadrature is used to evaluate the integrals in the residual equations. In Eqs. (16) and (17), the second term containing the penalty parameter (γ) are evaluated with two point Gaussian quadrature (reduced integration penalty formulation [28]). The motivation for reduced integration is given below. The matrix vector notation for the penalty finite element equations of the residuals, i.e., Eqs. (16)–(18) may be expressed in matrix vector notation as

$$(\mathbf{K_1} + \gamma\mathbf{K_2})\mathbf{a} = \mathbf{F}, \tag{19}$$

where $\mathbf{a}$ denotes the unknown vector, $\mathbf{K_1}$, $\mathbf{K_2}$ are the matrices obtained from the Jacobian of the residuals, As γ tends to a large value ($\sim 10^7$), the constraint equation (i.e., continuity equation) is satisfied better, which in turn causes the magnitude of $\mathbf{K_1}$ is negligible when compared with $\gamma\mathbf{K_2}$ resulting in

$$\mathbf{K_2 a} = \frac{\mathbf{F}}{\gamma}. \tag{20}$$

This implies that as γ tends to infinity, governing equations are left with only the constraint condition, i.e, the continuity equation. Hence, the contributions from the momentum and energy conservations are completely lost. In addition, as $\mathbf{K_2}$ is non-singular for large γ the resulting solution obtained from Eq. (20) is trivial. To obtain the non-trivial solutions for large $\gamma(\sim 10^7)$ the matrix $\mathbf{K_2}$ is needed to be a singular matrix. This is obtained by using two point Gaussian quadrature for $\mathbf{K_2}$ and three point Gaussian quadrature for $\mathbf{K_1}$. In the absence of the above reduced integration method velocities are underestimated [28].

The non-linear residual equations (16)–(18) are solved using a Newton–Raphson procedure to determine the

coefficients of the expansions in Eq. (15). At each iteration, the linear $(3N \times 3N)$ system

$$\mathbf{J}(\mathbf{a}^n)[\mathbf{a}^n - \mathbf{a}^{n+1}] = \mathbf{R}(\mathbf{a}^n), \tag{21}$$

is solved where n is the iterative index. The elements of the Jacobian matrix, $\mathbf{J}(\mathbf{a}^n)$ contains the derivatives of the residual equations with respect to velocity components (U_j)'s, (V_j)'s and the temperature (θ_j's) and $\mathbf{R}(\mathbf{a}^n)$ is the vector of residuals. The linear system for each iteration is based on efficient node numbering of the elements such that the jacobian forms a banded matrix. The iterative process is terminated with the convergence criterion $[\sum(R_i^{(j)})^2]^{0.5} \leqslant 10^{-5}$ using two-norm of residual vectors.

We have used nine node bi-quadratic elements with each element mapped using iso-parametric mapping [28] from X–Y to a unit square ξ–η domain.

Subsequently, the domain integrals in the residual equations are evaluated using nine node bi-quadratic basis functions in ξ–η domain as:

$$X = \sum_{i=1}^{9} X_i \Phi_i(\xi,\eta) \quad \text{and} \quad Y = \sum_{i=1}^{9} Y_i \Phi_i(\xi,\eta), \tag{22}$$

where $\Phi_i(\xi,\eta)$ are the local bi-quadratic basis functions on the ξ–η domain. The integrals in Eqs. (16)–(18) can be evaluated in ξ–η domain using following relationships:

$$\begin{bmatrix} \frac{\partial \Phi_i}{\partial X} \\ \frac{\partial \Phi_i}{\partial Y} \end{bmatrix} = \frac{1}{J} \begin{bmatrix} \frac{\partial Y}{\partial \eta} & -\frac{\partial Y}{\partial \xi} \\ -\frac{\partial X}{\partial \eta} & \frac{\partial X}{\partial \xi} \end{bmatrix} \begin{bmatrix} \frac{\partial \Phi_i}{\partial \xi} \\ \frac{\partial \Phi_i}{\partial \eta} \end{bmatrix}$$

and

$$\mathrm{d}X\mathrm{d}Y = J\mathrm{d}\xi\mathrm{d}\eta, \tag{23}$$

where

$$J = \frac{\partial(X,Y)}{\partial(\xi,\eta)} = \begin{vmatrix} \frac{\partial X}{\partial \xi} & \frac{\partial X}{\partial \eta} \\ \frac{\partial Y}{\partial \xi} & \frac{\partial Y}{\partial \eta} \end{vmatrix}.$$

4. Evaluation of stream function and Nusselt number

4.1. Stream function

The fluid motion is displayed using the stream function ψ obtained from velocity components U and V. The relationships between stream function, ψ [29] and velocity components for two-dimensional flows are

$$U = \frac{\partial \psi}{\partial Y}, \quad V = -\frac{\partial \psi}{\partial X}, \tag{24}$$

which yield a single equation

$$\frac{\partial^2 \psi}{\partial X^2} + \frac{\partial^2 \psi}{\partial Y^2} = \frac{\partial U}{\partial Y} - \frac{\partial V}{\partial X}. \tag{25}$$

Using the above definition of the stream function, the positive sign of ψ denotes anticlockwise circulation and the clockwise circulation is represented by the negative sign of ψ. Expanding the stream function (ψ) using the basis set $\{\Phi_k\}_{k=1}^{N}$ as $\psi = \sum_{k=1}^{N} \psi_k \Phi_k(X,Y)$ and the relation for U, V from Eq. (15), the Galerkin finite element method yield the following linear residual equations for Eq. (25).

$$R_i^{\mathrm{s}} = \sum_{k=1}^{N} \psi_k \int_\Omega \left[\frac{\partial \Phi_i}{\partial X}\frac{\partial \Phi_k}{\partial X} + \frac{\partial \Phi_i}{\partial Y}\frac{\partial \Phi_k}{\partial Y} \right] \mathrm{d}X\mathrm{d}Y + \sum_{k=1}^{n} U_k \int_\Omega \Phi_i \frac{\partial \Phi_k}{\partial Y}\,\mathrm{d}X\mathrm{d}Y - \sum_{k=1}^{n} V_k \int_\Omega \Phi_i \frac{\partial \Phi_k}{\partial X}\,\mathrm{d}X\mathrm{d}Y. \tag{26}$$

The no-slip condition is valid at all boundaries as there is no cross flow, hence $\psi = 0$ is used as residual equations at the nodes for the boundaries. The biquadratic basis function is used to evaluate the integrals in Eq. (26) and ψ's are obtained by solving the N linear residual equations (26).

4.2. Nusselt number

The heat transfer coefficient in terms of the local Nusselt number (Nu) is defined by

$$Nu = -\frac{\partial \theta}{\partial n}, \tag{27}$$

where n denotes the normal direction on a plane. The normal derivative is evaluated by the bi-quadratics basis set in ξ–η domain using Eqs. (22) and (23). The local Nusselt numbers at bottom wall (Nu_{b}) and at the side wall (Nu_{s}) are defined as

$$Nu_{\mathrm{b}} = -\sum_{i=1}^{9} \theta_i \frac{\partial \Phi_i}{\partial Y} \tag{28}$$

and

$$Nu_{\mathrm{s}} = -\sum_{i=1}^{9} \theta_i \frac{\partial \Phi_i}{\partial X}. \tag{29}$$

The average Nusselt numbers at the bottom and side walls are

$$\overline{Nu_{\mathrm{b}}} = \frac{\int_0^1 Nu_{\mathrm{b}}\,\mathrm{d}X}{X|_0^1} = \int_0^1 Nu_{\mathrm{b}}\,\mathrm{d}X \tag{30}$$

and

$$\overline{Nu_{\mathrm{s}}} = \frac{\int_0^1 Nu_{\mathrm{s}}\,\mathrm{d}Y}{Y|_0^1} = \int_0^1 Nu_{\mathrm{s}}\,\mathrm{d}Y. \tag{31}$$

5. Results and discussion

5.1. Numerical tests

The computational domain consists of 20×20 bi-quadratic elements which correspond to 41×41 grid points.

The bi-quadratic elements with lesser number of nodes smoothly capture the non-linear variations of the field variables which are in contrast with finite difference/finite volume solutions available in Refs. [10,18]. In order to assess the accuracy of our numerical procedure, we have tested our algorithm based on the grid size (41×41) for a square enclosure with a side wall heated and the results are in well agreement with the work of Lauriat and Prasad [18]. Comparisons are not shown here for the brevity of the manuscript.

Computations have been carried out for various values of $Ra = 10^3$–10^6 and $Pr = 0.71$–10 with uniform and non-uniform bottom wall heating where side walls are cooled and the top wall is well insulated. The jump discontinuities in Dirichlet type of wall boundary conditions at the corner points (see Fig. 1) correspond to computational singularities. In particular, the singularity at the corner nodes of the bottom wall needs special attention. The grid size dependent effect of the temperature discontinuity at the corner points upon the local (and the overall) Nusselt numbers tend to increase as the mesh spacing at the corner is reduced. One of the ways for handling the problem is assuming the average temperature of the two walls at the corner and keeping the adjacent grid-nodes at the respective wall temperatures. Alternatively, based on earlier work by Ganzarolli and Milanez [30], this procedure is still grid dependent unless a sufficiently refined mesh is implemented. Accordingly, once any corner formed by the intersection of two differently heated boundary walls is assumed at the average temperature of the adjacent walls, the optimal grid size obtained for each configuration corresponds to the mesh spacing over which further grid refinements lead to grid invariant results in both heat transfer rates and flow fields. The similar observations are also reported in an earlier work [31].

In the current investigation, Gaussian quadrature based finite element method provides the smooth solutions at the interior domain including the corner regions as evaluation of residual depends on interior gauss points and thus the effect of corner nodes are less pronounced in the final solution. In general, the Nusselt numbers for finite difference/finite volume based methods are calculated at any surface using some interpolation functions which are now avoided in the current work. The present finite element approach offers special advantage on evaluation of local Nusselt number at the bottom and side walls as the element basis functions are used to evaluate the heat flux. Note that, the number of grid points in the current study is 41×41 and these nodal numbers are in agreement with the number of grid points 33×33 as illustrated by Corcione [31]. In addition, the percent changes of the average Nusselt numbers ($\overline{Nu}_b$ and $\overline{Nu}_s$) and the maximum horizontal and vertical dimensionless velocity components at an assigned vertical and horizontal plane across the cavity are within 0.1–1%.

5.2. Effects of Darcy number: uniform heating at bottom wall

Figs. 2–5 illustrate the stream function and isotherm contours of the numerical results for various $Ra = 10^3$–10^6, $Da = 10^{-5}$–10^{-3} and $Pr = 0.71$–10 when the bottom wall is uniformly heated. In general, the fluid circulation is strongly dependent on Darcy number as we have seen in Figs. 2–5. Fig. 2 illustrates the stream function and temperature contours for $Da = 10^{-5}$ and $Ra = 10^6$, and the flow is seen to be very weak as observed from stream function contours. Therefore, the temperature distribution is similar to that with stationary fluid and the heat transfer is due to purely conduction. During conduction dominant heat transfer, the temperature contours with $\theta = 0.1$ occur symmetrically near the side walls of the enclosure. The other temperature contours with $\theta \geqslant 0.2$ are smooth curves which span the entire enclosure and they are generally symmetric with respect to the vertical symmetric line. As Darcy number increases to 10^{-4}, the strength of flow is increased at $Ra = 10^6$. As expected due to the cold

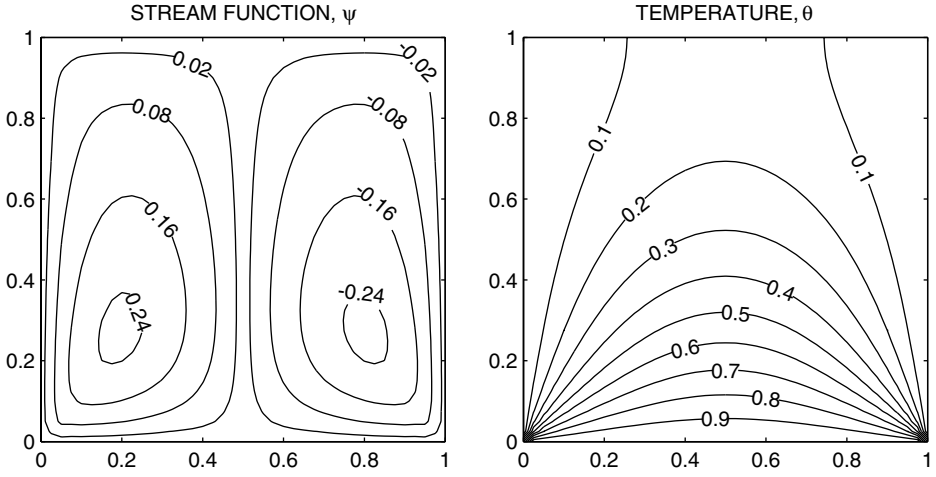

Fig. 2. Contour plots for uniform bottom heating, $\theta(X,0) = 1$, with $Pr = 0.71$ and $Ra = 10^6$, $Da = 10^{-5}$. Clockwise and anti-clockwise flows are shown via negative and positive signs of stream functions, respectively.

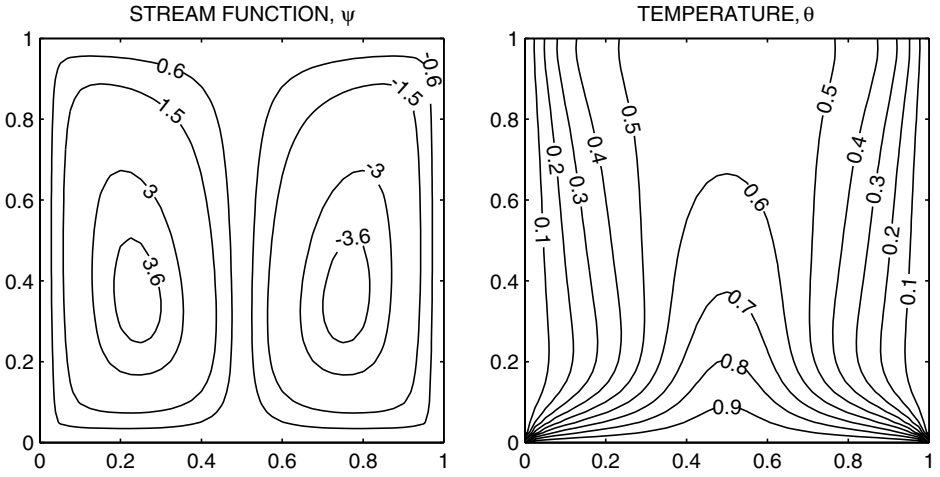

Fig. 3. Contour plots for uniform bottom heating, $\theta(X,0) = 1$, with $Pr = 0.71$ and $Ra = 10^6$, $Da = 10^{-4}$. Clockwise and anti-clockwise flows are shown via negative and positive signs of stream functions, respectively.

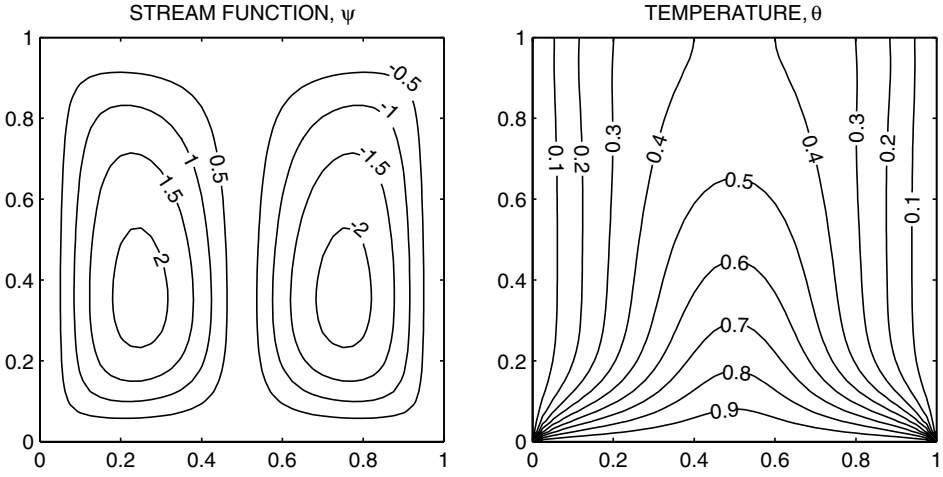

Fig. 4. Contour plots for uniform bottom heating, $\theta(X,0) = 1$, with $Pr = 0.71$ and $Ra = 7 \times 10^4$, $Da = 10^{-3}$. Clockwise and anti-clockwise flows are shown via negative and positive signs of stream functions, respectively.

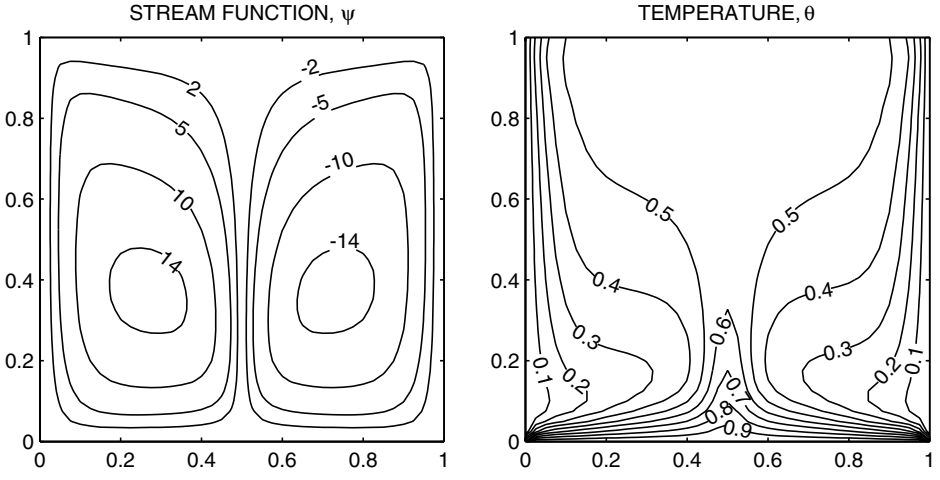

Fig. 5. Contour plots for uniform bottom heating, $\theta(X,0) = 1$, with $Pr = 0.71$ and $Ra = 10^6$, $Da = 10^{-3}$. Clockwise and anti-clockwise flows are shown via negative and positive signs of stream functions, respectively.

vertical walls, fluids rise up from middle portion of the bottom wall and flow down along the two vertical walls forming two symmetric rolls with clockwise and anti-clockwise rotations inside the cavity. The stronger circulation causes the temperature contours to be concentrated near the side walls and near the edges of bottom wall which may result in greater heat transfer rate due to convection. Note that, at $Da = 10^{-4}$, the conduction dominant heat transfer mode would occur upto $Ra = 5 \times 10^5$.

During $Da = 10^{-3}$, flow is a very strong function of Ra and the conduction dominant heat transfer occurs upto $Ra = 7 \times 10^4$. During conduction dominant mode, the temperature profile is similar to that in Fig. 2. At $Da = 10^{-3}$ and $Ra = 7 \times 10^4$, the circulation near the central regimes are stronger and consequently, the temperature contour with $\theta = 0.2$ (in Fig. 2) starts getting shifted towards the side wall and they break into two symmetric contour lines (Fig. 4). The presence of significant convection is also exhibited in other temperature contours lines which start getting deformed and pushed towards the side wall. The conduction dominant heat transfer will be illustrated later via average Nusselt number vs. Rayleigh number plot and the critical Rayleigh number would demonstrate the significant effect of convective heat transfer.

As Rayleigh number increases to 10^6 with $Da = 10^{-3}$, the buoyancy driven circulation inside the cavity is also increased as seen from greater magnitudes of the stream functions (Fig. 5). The circulations are greater near the center and least at the wall due to no slip boundary conditions. The greater circulation in each half of the box follows a progressive wrapping around the centers of rotation, and a more and more pronounced compression of the isotherms toward the boundary surfaces of the enclosures occurs. Consequently, at $Da = 10^{-3}$, the temperature gradients near both the bottom and side walls tend to be significant to develop the thermal boundary layer. Due to greater circulations near the central core at the top half of the enclosure, there are small gradients in temperature whereas a large stratification zone of temperature is observed at the vertical symmetry line due to stagnation of flow. Fig. 2 shows that the thermal boundary layer develops approximately 75% within the cavity for $Da = 10^{-5}$, whereas for $Da = 10^{-3}$, the isotherms presented in Fig. 5 indicate that the thermal boundary layer almost develops throughout the entire cavity. Comparative studies for the increase of Pr from 0.71 to 10 show that the values of stream function and isotherms in the core cavity increase. Due to greater circulation at $Pr = 10$, the zone of stratification of temperature at the central symmetric line is reduced (figures are not shown).

5.3. Effects of Darcy number: non-uniform heating at bottom wall

Stream function contours and isotherms are displayed in Figs. 6 and 7 for $Da = 10^{-4}$–10^{-3}, $Ra = 10^6$ and $Pr = 0.71$ when the bottom wall is non-uniformly heated. As seen in Figs. 2–5, uniform heating of the bottom wall causes a finite discontinuity in Dirichlet type of boundary conditions for the temperature distribution at the edges of the bottom wall. In contrast, the non-uniform heating removes the singularities at the edges of the bottom wall and provides a smooth temperature distribution in the entire cavity. For $Da = 10^{-4}$ and $Pr = 0.71$, the temperature contours as seen in Fig. 6 are similar to that with uniform heating case as seen in Fig. 3. The conduction dominant heat transfer mode is upto $Ra = 5 \times 10^5$ which is similar to that with uniform heating case. It is interesting to note that, the temperature at the bottom wall is non-uniform and maxima in temperature occurs at the center. Therefore, the greater heat transfer rate will occur at the center and the detailed analysis will be illustrated in the following section.

At $Da = 10^{-3}$, the circulation pattern is qualitatively similar to the uniform heating case with the identical situation (Fig. 7). Due to non-uniform bottom heating, the heating rate near the wall is generally lower which induce

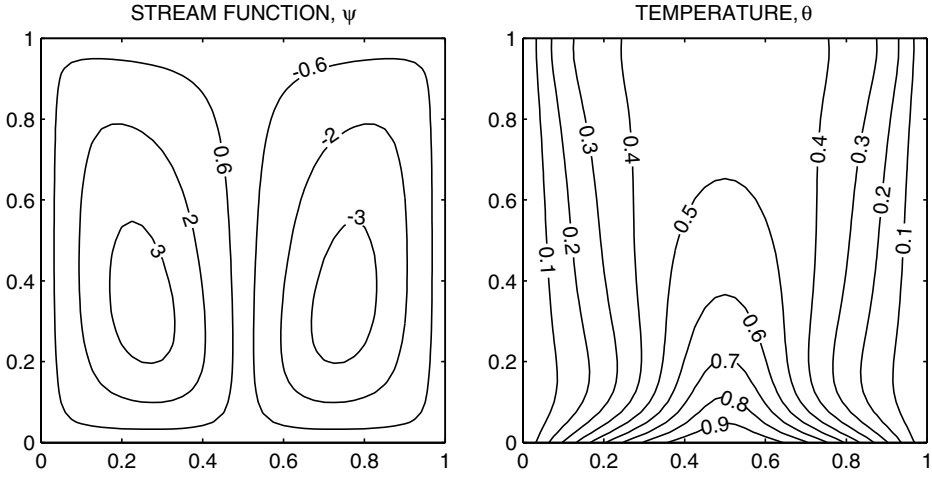

Fig. 6. Contour plots for non-uniform bottom heating, $\theta(X,0) = \sin(\pi X)$, with $Pr = 0.71$ and $Ra = 10^6$, $Da = 10^{-4}$. Clockwise and anti-clockwise flows are shown via negative and positive signs of stream functions, respectively.

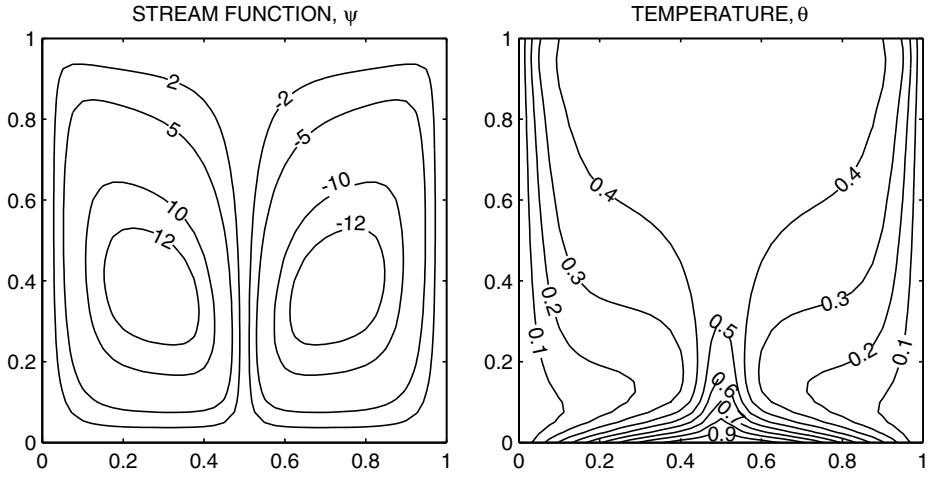

Fig. 7. Contour plots for non-uniform bottom heating, $\theta(X,0) = \sin(\pi X)$, with $Pr = 0.71$ and $Ra = 10^6$, $Da = 10^{-3}$. Clockwise and anti-clockwise flows are shown via negative and positive signs of stream functions, respectively.

less buoyancy effect resulting in less thermal gradient throughout the domain. The conduction dominant heat transfer will occur upto $Ra = 3 \times 10^5$ which is in contrast with the uniform heating case where conduction regime is valid within $Ra = 7 \times 10^4$. The uniformity in temperature distribution and least temperature gradient are still observed at the central core regime within the top half of the domain. The less buoyancy effect also leads to a large zone of stratification of temperature at the vertical line of symmetry (Fig. 7). However, compared to uniform heating cases, the values of temperature contours are less near the central and top portion of the enclosure for non-uniform heating case. The greater values of temperature contours are highly dense near the bottom wall which may indicate a greater local heating rate compared to the uniform heating case as seen in Fig. 5.

5.4. Heat transfer rates: local and average Nusselt numbers

Fig. 8 display the effects of Ra and Da on the local Nusselt numbers at the bottom and side walls (Nu_b, Nu_s) for $Pr = 0.71$ and 10. For uniform heating of the bottom wall, the heat transfer rate or Nu_b is very high at the edges of the bottom wall due to the discontinuities present in the temperature boundary conditions at edges and heat transfer rate reduces towards the center of the bottom wall with its minimum value at the center (Fig. 8(a)). On the contrary, for $Da = 10^{-5}$ with non-uniformly heated bottom wall, Nu_b increases from zero at both the edges of the bottom wall towards the center with its maximum value at the center. Further for $Da \geqslant 10^{-4}$, the non-uniform heating produces a sinusoidal type of local heat transfer rate with its minimum values at the edges as well as at the center of the bottom wall. The physical reason of this type of behavior is due to the higher values of stream function (i.e., high flow rate) for $Da \geqslant 10^{-4}$ in the middles of the first and second half of the cavity. Due to the variations

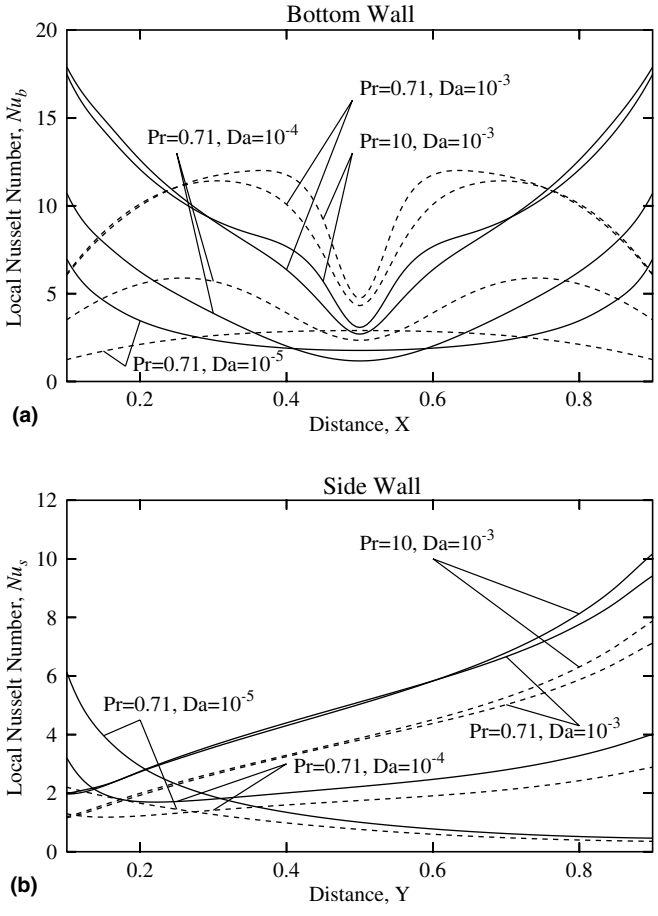

Fig. 8. Variation of local Nusselt number with distance (a) at the bottom wall (b) at the side wall for uniform heating (—) and non-uniform heating (– – –).

of Pr from 0.71 to 10, the local Nusselt number at the bottom wall (Nu_b) increases slightly as seen in Fig. 8(a). It is interesting to note that for all regimes of Darcy and Rayleigh numbers, the non-uniform heating enhances the heat

transfer at the central regime only. The temperature contours diverge from the corner points toward the central vertical line for uniform heating cases and therefore local Nusselt number is a monotonically decreasing function with the distance. In contrast, for non-uniform heating cases the temperature contours are compressed around the intermediate zones between corner and the vertical line of symmetry at the bottom wall and local Nusselt number is maximum at around $X = 0.4$ and 0.6.

Fig. 8(b) illustrates the heat transfer rate at the side wall. The local Nusselt number (Nu_s) is found to be decreasing with distance at the side or cold wall for $Da = 10^{-5}$, $Pr = 0.71$ for both uniform and non-uniform heating cases. It is interesting to note that, the heat transfer rate is initially decreased and later increased with distance for $Da \geqslant 10^{-4}$ with $Pr = 0.71$ and 10. At higher Rayleigh number, the significant circulation as seen in Figs. 3–7 results in dense contours at the top portion of the side walls and these dense temperature contours are in contrast with the conduction dominant cases as seen in Fig. 2. Further, it is observed that, the temperature contours are compressed towards the side walls away from the corner points at the bottom specially for $Da = 10^{-3}$. Therefore, the heat fluxes are enhanced at the regimes away from bottom corner points. The heat transfer rates are qualitatively similar, but reduced for non-uniform bottom wall heating cases as compared to the uniform heating cases. Similar to the bottom wall, the local Nusselt number shows slightly increased heat transfer at the top portion of the side wall for $Pr = 10$.

The overall effects upon the heat transfer rates are displayed in Fig. 9(a)–(d), where the distributions of the average Nusselt number of bottom and side walls, respectively, are plotted vs the logarithmic Rayleigh number. The average Nusselt numbers are obtained using Eqs. (30) and (31) where the integral is evaluated using Simpson's 1/3 rule. Note that, Fig. 9(a) and (b) (Cases a and b) illustrate uniform heating cases and Fig. 9(c) and (d) (Cases c and d) illustrate non-uniform heating cases. For all these cases, it is observed that average Nusselt numbers for both the bottom and side walls remain constant for $Da = 10^{-5}$ during the entire Rayleigh number regime upto $Ra = 10^6$. As

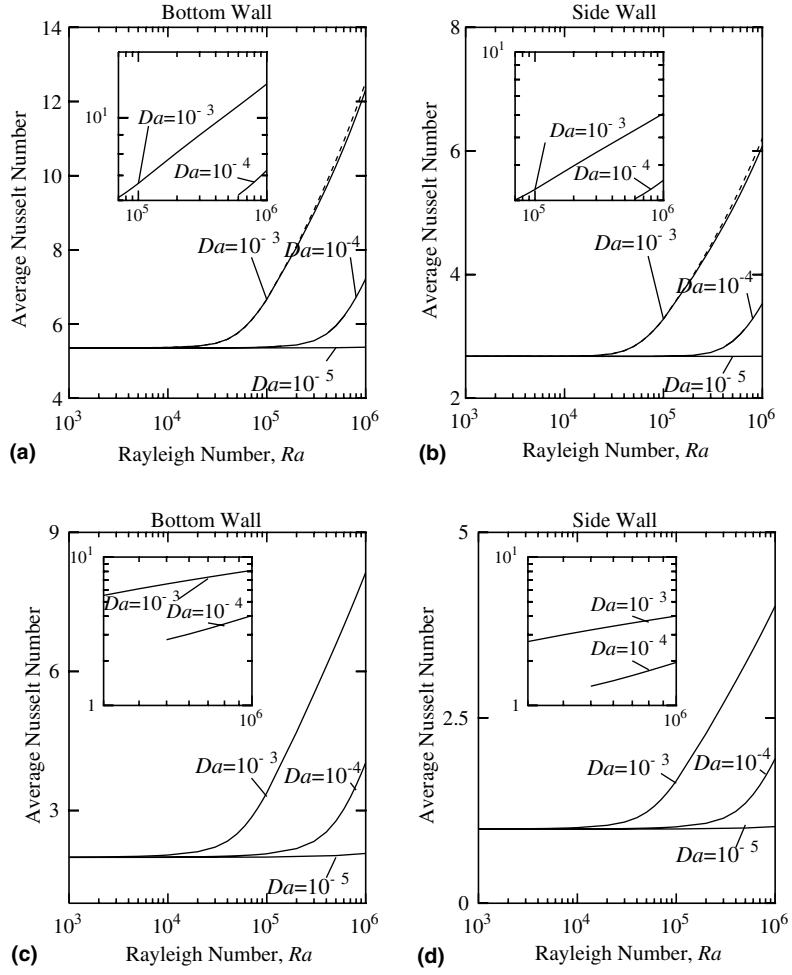

Fig. 9. Variation of average Nusselt number with Rayleigh number for uniform heating [(a) and (b)] and non-uniform heating [(c) and (d)] with $Pr = 0.71$; (—) and $Pr = 10$; (---) (shown for (a) and (b)). The insets show the log–log plot of average Nusselt number vs. Rayleigh number for convection dominant regimes.

Da increases, the conduction dominant heat transfer regime is narrowed down as conduction dominance occurs upto $Ra = 5\times10^5$ and $Ra = 7\times10^4$ for $Da = 10^{-4}$ and $Da = 10^{-3}$, respectively, during uniform heating case. In contrast for non-uniform heating case, $Ra = 5\times10^5$ and $Ra = 3\times10^5$ are the critical Rayleigh numbers for $Da = 10^{-4}$ and $Da = 10^{-3}$, respectively. Note that, larger Rayleigh number regime of heat conduction mode corresponding to smaller Darcy numbers produces overall lower heat transfer rate both for uniform and non-uniform heating cases. The insets show the log–log plot for average Nusselt number vs. Rayleigh number for convection dominant regimes. The log–log linear plot is obtained with more than 20 data set. A least square curve is fitted and the overall error is limited within 1%. The following correlations with $Pr = 0.71$ are obtained for cases a and b (uniform heating) and c and d (non-uniform heating) as follows:

Cases a and b: uniform heating

$$\begin{aligned}\overline{Nu_b} &= 2\overline{Nu_s}\\ &= 0.150Ra^{0.280}, \quad Ra \geqslant 5\times10^5,\ Da = 10^{-4}\\ &= 0.316Ra^{0.265}, \quad Ra \geqslant 7\times10^4;\ Da = 10^{-3}.\end{aligned} \tag{32}$$

Cases c and d: non-uniform heating

$$\begin{aligned}\overline{Nu_b} &= 2\overline{Nu_s}\\ &= 0.0022Ra^{0.543}, \quad Ra \geqslant 5\times10^5;\ Da = 10^{-4}\\ &= 0.077Ra^{0.338}, \quad Ra \geqslant 3\times10^5;\ Da = 10^{-3}.\end{aligned} \tag{33}$$

6. Conclusions

The prime objective of the current investigations is to study the effect of continuous and discontinuous thermal boundary conditions on the flow and heat transfer characteristics due to natural convection within a porous square enclosure. The momentum transfer in the porous region is modeled by using Darcy–Forchheimer law. The penalty finite element method helps to obtain smooth solutions in terms of stream function and isotherm contours for wide ranges of Da, Pr and Ra with uniform and non-uniform heating of the bottom wall. We have demonstrated the formation of boundary layers for both the heating cases and it is observed that thermal boundary layer is developed approximately 75% within the cavity for uniform heating whereas the boundary layer is approximately 60% for non-uniform heating when $Ra = 10^6$, $Da = 10^{-5}$, and $Pr = 0.71$. The heat transfer rate is very high at the edges of the bottom wall and decreases to a minimum value at the center due to uniform heating which contrast the lower heat transfer rate at the edges due to non-uniform heating for $Ra = 10^6$ and $Da \geqslant 10^{-4}$. We observed the conduction dominant heat transfer modes for $Ra \leqslant 7\times10^4$ during uniform heating of bottom wall whereas the conduction dominant heat transfer is observed for $Ra \leqslant 3\times10^5$ for non-uniform heating corresponding to $Da = 10^{-4}$.

At the onset of convection dominant mode, the temperature contour lines get compressed toward the side walls and they tend to get deformed towards the upward direction. During $Ra = 10^6$ and $Da \geqslant 10^{-4}$, the thermal boundary layer is developed near the bottom and side walls and the central regime near the top surface has least temperature gradient for both uniform and non-uniform heating cases. The local Nusselt numbers at the bottom and side walls represent various interesting heating features. The local Nusselt number at the bottom wall is least at the center for uniform heating and there are two least heat transfer zones at the center and the corner points for non-uniform heating. The non-uniform heating exhibits greater heat transfer rates at the center of the bottom wall than that with uniform heating case for all Rayleigh number regimes. The local Nusselt number at the side wall is found to be decreased with distance for conduction dominant heat transfer whereas due to highly dense contour lines near the top portion of the side wall, the local Nusselt number is found to be increased for both uniform and non-uniform heating cases. The average Nusselt number illustrates overall lower heat transfer rates for non-uniform heating cases. It is observed that, the heat transfer is primarily due to conduction for $Da \leqslant 10^{-5}$ irrespective of Ra and as Da increases, the conduction dominant regime is shortened with Ra. The average Nusselt number is found to be following power law variation with Rayleigh number for convection dominant regimes. The non-uniform or sinusoidal heating may be employed in small regime followed by a uniform heating and this combination may be suitable to achieve enhanced heat transfer effects. This analysis is a subject of our ongoing research.

Acknowledgements

Authors express sincere thanks to the reviewer for the valuable suggestions and comments on our paper. One of the authors, T. Paul is thankful to Department of Science and Technology, New Delhi, for the financial assistance.

References

[1] S. Kaviany, Principles of Heat Transfer in Porous Media, Springer-Verlag, New York, 1995.
[2] D.A. Nield, A. Bejan, Convection in Porous Media, Springer-Verlag, New York, 1999.
[3] D.B. Ingham, I. Pop (Eds.), Transport Phenomena in Porous Media, Pergamon, Oxford, 1998, vol. II, 2002; vol. III, 2005.
[4] K. Vafai, Handbook of Porous Media, Marcel Dekker, New York, 2000.
[5] I. Pop, D.B. Ingham, Convective Heat Transfer, Mathematical and Computational Modeling of Viscous Fluids and Porous Media, Pergamon, Oxford, 2001.
[6] A. Bejan, A.D. Kraus (Eds.), Heat Transfer Handbook, Wiley, New York, 2003.
[7] D.B. Ingham, A. Bejan, E. Mamut, I. Pop (Eds.), Emerging Technologies and Techniques in Porous Media, Kluwer, Dordrecht, 2004.

[8] A. Bejan, I. Dincer, S. Lorente, A.F. Miguel, A.H. Reis, Porous and Complex Flow Structures in Modern Technologies, Springer, New York, 2004.
[9] K.L. Walker, G.M. Homsy, Convection in porous cavity, J. Fluid Mech. 87 (1978) 449–474.
[10] T.W. Tong, E. Subramanian, Boundary layer analysis for natural convection in porous enclosure: use of the Brinkman-extended Darcy model, Int. J. Heat Mass Transfer 28 (1985) 563–571.
[11] G. Lauriat, V. Prasad, Natural convection in a vertical porous cavity: a numerical study for Brinkman-extended Darcy formulation, Trans. ASME J. Heat Transfer 109 (1987) 295–320.
[12] H.C. Brinkman, On the permeability of media consisting of closely packed porous particles, Appl. Sci. Res. 1 (1947) 81–86.
[13] K. Vafai, C.L. Tien, Boundary and inertia effects on flow and heat transfer in porous media, Int. J. Heat Mass Transfer 24 (1981) 195–203.
[14] C.K. Chen, C.R. Lin, Natural convection from an isothermal vertical surface embedded in a thermally stratified high-porosity medium, Int. J. Eng. Sci. 33 (1995) 131–138.
[15] D. Poulikakos, A. Bejan, The departure from Darcy flow in natural convection in a vertical porous layer, Phys. Fluids 28 (1985) 3477–3484.
[16] D. Poulikakos, A departure from the Darcy model in boundary layer natural convection in a vertical porous layer with uniform heat flux, Trans. ASME J. Heat Transfer 107 (1985) 716–720.
[17] C. Beckermann, R. Viskanta, S. Ramadhyani, A numerical study of non-Darcian natural convection in a vertical enclosure filled with a porous medium, Numer. Heat Transfer 10 (1986) 557–570.
[18] G. Lauriat, V. Prasad, Non-Darcian effects on natural convection in a vertical porous enclosure, Int. J. Heat Mass Transfer 32 (1989) 2135–2148.
[19] A.A. Mohammad, Non-equilibrium natural convection in a differentially heated cavity filled with a saturated porous matrix, Trans. ASME J. Heat Transfer 122 (2000) 380–384.
[20] A.C. Baytas, I. Pop, Free convection in a square porous cavity using a thermal non-equilibrium model, Int. J. Therm. Sci. 41 (2002) 861–870.
[21] N.H. Saeid, I. Pop, Viscous dissipation effects on free convection in a porous cavity, Int. Commun. Heat Mass Transfer 31 (2004) 723–732.
[22] R. Horne, M. O'sullivan, Oscillatory convection in a porous medium heated from below, J. Fluid Mech. 66 (1974) 339–352.
[23] J.P. Caltagirone, Thermoconvective instabilities in a horizontal porous layer, J. Fluid Mech. 72 (1975) 269–287.
[24] J.M. Straus, Large amplitude convection in porous media, J. Fluid Mech. 64 (1974) 51–63.
[25] W.J. Minkowycz, E.M. Sparrow, G.E. Schneider, R.H. Fletcher, Handbook of Numerical Heat Transfer, Wiley, New York, 1988.
[26] Z.-G. Du, E. Bilgen, Natural convection in vertical cavities with internal heat generating porous medium, Wärme-und Stoffübertr. 27 (1992) 149–155.
[27] T. Basak, K.G. Ayappa, Influence of internal convection during microwave thawing of cylinders, AIChE J. 47 (2001) 835–850.
[28] J.N. Reddy, An Introduction to the Finite Element Method, McGraw-Hill, New York, 1993.
[29] G.K. Batchelor, An Introduction to Fluid Dynamics, Cambridge University Press, 1993.
[30] M.M. Ganzarolli, L.F. Milanez, Natural convection in rectangular enclosures heated from below and symmetrically cooled from the sides, Int. J. Heat Mass Transfer 38 (1995) 1063–1073.
[31] M. Corcione, Effects of the thermal boundary conditions at the sidewalls upon natural convection in rectangular enclosures heated from below and cooled from above, Int. J. Therm. Sci. 42 (2003) 199–208.